

## The 4.5 Å Structure of Human AQP2

Andreas D. Schenk<sup>1</sup>, Paul J. L. Werten<sup>1</sup>, Simon Scheuring<sup>2</sup>  
Bert L. de Groot<sup>3</sup>, Shirley A. Müller<sup>1</sup>, Henning Stahlberg<sup>4</sup>  
Ansgar Philippsen<sup>1</sup> and Andreas Engel<sup>1\*</sup>

<sup>1</sup>M. E. Müller Institute for  
Microscopy, Biozentrum  
University of Basel  
Klingelbergstrasse 70, 4056  
Basel, Switzerland

<sup>2</sup>Institut Curie, UMR-CNRS  
168 and LRC-CEA 34V, 11 rue  
Pierre et Marie Curie, 75231  
Paris Cedex 05, France

<sup>3</sup>Computational Biomolecular  
Dynamics Group  
Max-Planck-Institute for  
Biophysical Chemistry, Am  
Fassberg 11, 37077 Göttingen  
Germany

<sup>4</sup>Molecular and Cellular  
Biology, University of  
California, 1 Shields Avenue  
Davis, CA 95616, USA

\*Corresponding author

Located in the principal cells of the collecting duct, aquaporin-2 (AQP2) is responsible for the regulated water reabsorption in the kidney and is indispensable for the maintenance of body water balance. Disregulation or malfunctioning of AQP2 can lead to severe diseases such as nephrogenic diabetes insipidus, congestive heart failure, liver cirrhosis and pre-eclampsia. Here we present the crystallization of recombinantly expressed human AQP2 into two-dimensional protein-lipid arrays and their structural characterization by atomic force microscopy and electron crystallography. These crystals are double-layered sheets that have a diameter of up to 30  $\mu\text{m}$ , diffract to 3  $\text{\AA}^{-1}$  and are stacked by contacts between their cytosolic surfaces. The structure determined to 4.5 Å resolution in the plane of the membrane reveals the typical aquaporin fold but also a particular structure between the stacked layers that is likely to be related to the cytosolic N and C termini.

© 2005 Elsevier Ltd. All rights reserved.

**Keywords:** aquaporin; atomic force microscopy; electron crystallography; nephrogenic diabetes insipidus; 2D crystallization

### Introduction

As water is the major constituent of all forms of life, maintaining water homeostasis is crucial for all living organisms. While water passes through pure lipid bilayers with high activation energy ( $E_a > 10$  kcal/mol), the rapid flow of water through specialized membranes, e.g. in the kidneys, occurs with an  $E_a < 5$  kcal/mol. Members of the aquaglyceroporin family facilitate this efficient transport of water and small solutes across biological membranes.<sup>1–5</sup> Phylogenetic analyses have revealed two distinct subfamilies, the aquaporin (AQP) and the glyceroporin (GLP) subfamilies. Members of the former are highly specific for water, but members of the latter also permeate

small solutes such as glycerol.<sup>6</sup> Aquaglyceroporins are homo-tetrameric membrane proteins, with each monomer comprising six transmembrane helices forming a right-handed bundle that houses an independent channel. Site-directed mutagenesis on the functional loops containing the NPA motifs has led to the “hourglass” model in which the intracellular and the extracellular NPA loops project back into the membrane bilayer where their intersection forms a narrow aperture.<sup>7</sup> Two unusual half-helices in these loops emanate outwards from the two highly conserved stacked proline residues in the middle of the membrane. These half-helices form a pseudo seventh helix, and together with helices 1, 2, 4 and 5 build the framework for the actual channel.<sup>8</sup> Altogether six atomic mammalian aquaporin structures (human AQP1 (1FQY;<sup>8</sup> 1H6I,<sup>9</sup> 1IH5<sup>10</sup>), bovine AQP1 (1J4N<sup>11</sup>) and AQP0 (1SOR,<sup>12</sup> 1YMG<sup>13</sup>)), and four structures of bacterial aquaglyceroporins (GlpF (1FX8;<sup>14</sup> 1LDA, 1LDI<sup>15</sup>) and AqpZ (1RC2<sup>16</sup>)) have been deposited in the Protein Data Bank.

In the human kidney, several members of the

Abbreviations used: AQP2, aquaporin-2; HT, His-tagged; LPR, lipid-to-protein ratio; AFM, atomic force microscopy; MPA, mass-per-area; STEM, scanning transmission electron microscopy.

E-mail address of the corresponding author:  
andreas.engel@unibas.ch

aquaporin family are responsible for water reabsorption. Of the 180 liters of pro-urine filtered daily, 90% is reabsorbed *via* AQP1, which is expressed in the apical and basolateral membranes of epithelial cells in the proximal tubules and descending limbs of Henle. The remaining water reabsorption takes place in the collecting duct. It is mediated by AQP2 in the apical membrane and by AQP3 and AQP4 in the basolateral membrane of the principal cells of the collecting duct, and is controlled by the anti-diuretic hormone vasopressin (AVP).<sup>17–19</sup> Binding of AVP to its receptor (V2R) on the basolateral side of the collecting duct cells leads to activation of cAMP-dependent protein kinase A, which phosphorylates AQP2 at C-terminal residue Ser256. This promotes the redistribution of AQP2 from intracellular storage vesicles to the apical plasma membrane, where it can exert its function as a water channel. Removal of AVP reverses this process. Disregulation or malfunctioning of AQP2 can lead to a variety of severe diseases, such as nephrogenic diabetes insipidus<sup>20–23</sup> congestive heart failure,<sup>23–26</sup> liver cirrhosis<sup>26–29</sup> and pre-eclampsia,<sup>23,26,30,31</sup> showing the physiological importance of this protein.

The double-layered two-dimensional (2D) AQP2 crystals presented here diffract to  $3 \text{ \AA}^{-1}$ . They were characterized by atomic force microscopy (AFM), transmission electron microscopy (TEM) and electron crystallography, and the structure of AQP2 was determined to a resolution of 4.5 Å in the plane of the membrane and 7 Å perpendicular to it. This 3D potential map was calculated using information from electron images only, and is the first medium resolution structure of a recombinantly expressed human membrane channel. Since both the N and C termini of AQP2 are trapped between the two crystal layers, their structure is sufficiently well ordered for crystallographic analysis. This information will help to understand the regulated shuttling of AQP2 to the apical membrane of the principal collecting duct cells.

## Results and Discussion

### Crystallization

Solubilized and highly purified N-terminally

His-tagged AQP2 (HT-AQP2), previously shown to be functionally active and to exist as a tetramer,<sup>32</sup> was reconstituted into crystalline protein-lipid arrays. Initial crystallization trials were conducted in dialysis buttons at room temperature, while the most favorable conditions were determined using a temperature-controlled dialysis machine.<sup>33</sup> Table 1 summarizes the conditions tested and the optimal conditions found.

At pH 6.0, HT-AQP2 readily incorporated into proteoliposomes in the presence of *Escherichia coli* lipids or heart polar lipids, but not with dioleoylphosphatidylcholine (DOPC) or dimyristoylphosphatidylcholine (DMPC). Proteoliposomes of *E. coli* lipids clustered together more strongly than those containing heart polar lipids. At pH 5.0 only aggregates were found. When the pH was between 7.0 and 8.0 the vesicles were smaller, were mixed with tube-like structures and also had a propensity to aggregate. The protein concentration had a significant influence on the crystallinity of reconstituted HT-AQP2: Higher protein concentrations resulted in better-ordered protein-lipid arrays. The highest protein concentration used was 0.7 mg/ml for which the optimal lipid-to-protein ratio (LPR) was 0.5. Addition of  $\text{Mg}^{2+}$ , either in the form of  $\text{MgCl}_2$  or as  $\text{MgSO}_4$ , dramatically improved the crystal quality. For reasons unknown,  $\text{MgCl}_2$  seemed to work slightly better for *E. coli* lipids, whereas  $\text{MgSO}_4$  gave better results for heart polar lipids. At concentrations above 5 mM, however,  $\text{Mg}^{2+}$  led to severe aggregation of the HT-AQP2 protein. It is not clear whether the His-tag at the protein's N terminus was responsible for this phenomenon, since similar aggregation previously observed for His-tagged AqpZ was also found after proteolytic elimination of the His-tag.<sup>34</sup> The concentration of NaCl had little influence on crystallinity, and was found to be optimal at 100 mM. Of the other additives tested, only histidine had a positive effect on crystal quality. At a concentration of 5 mM, it improved long-range crystallinity and reduced stacking of the 2D crystals.

However, the best 2D crystals were produced when a temperature-controlled dialysis machine was used for detergent removal. Instead of the round vesicle-like structures observed after using dialysis buttons (Figure 1(a)), large rectangular

**Table 1.** Summary of 2D-crystallization experiments

Parameter	Range tested	Optimal condition
Lipid type	DOPC, DMPC, <i>E. coli</i> lipids, Heart polar lipids	Heart polar lipids or <i>E. coli</i> lipids
Protein concentration	0.35–0.7 mg/ml	0.7
LPR	0.4–1.2	0.5
Buffer	Citric acid, Mes, $\text{K}_2\text{HPO}_4/\text{Na}_2\text{HPO}_4$ , Tris	20 mM Mes
pH	5.0–8.0	6.0
NaCl	100–600 mM	100 mM
$\text{MgCl}_2$ or $\text{MgSO}_4$	0–20 mM	5 mM
DTT	0–10 mM	–
$\text{NiCl}_2$	0–10 mM	–
$\text{CaCl}_2$	0–10 mM	–
Histidine	0–50 mM	5 mM

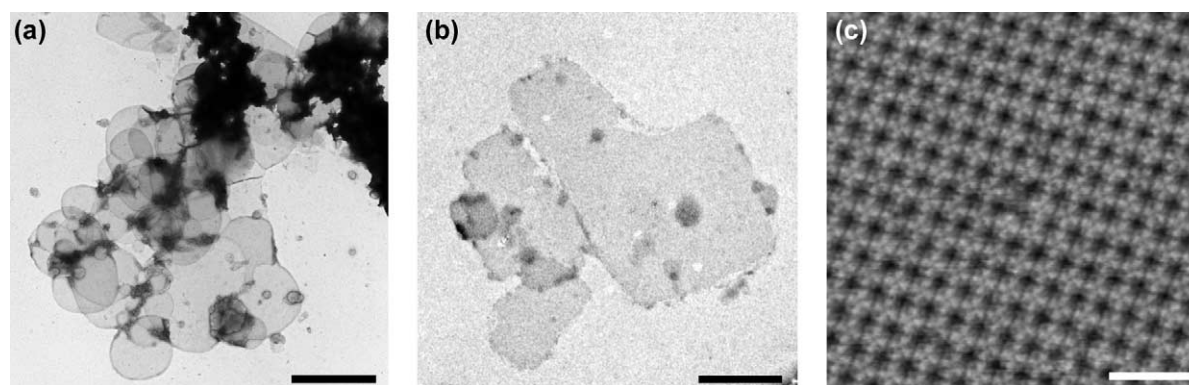


**Figure 1.** Electron microscopy of 2D AQP2 crystals. (a) Electron micrograph of a negatively stained sample of AQP2 2D crystals produced in dialysis buttons. Scale bar corresponds to 2  $\mu\text{m}$ . The 2D crystals appear as vesicle-like structures, often clustered together and attached to aggregates. (b) Cryo-electron microscopic overview of AQP2 2D crystals obtained under optimized conditions in a dialysis machine. 2D crystals appear as large mono-crystalline rectangular protein-lipid arrays. Scale bar corresponds to 2  $\mu\text{m}$ . (c) High-resolution AFM topograph of an AQP2 crystal sheet recorded at low force in an optimized imaging buffer. Scale bar corresponds to 150 Å.

protein-lipid 2D crystals were obtained (Figure 1(b)), whose surface topography recorded by AFM revealed mono-crystalline arrays of highly ordered tetramers (Figure 1(c)). Although the initial order of crystals prepared using heart polar lipid was slightly higher than that of crystals formed in the presence of *E. coli* lipids, these differences disappeared after a few weeks of storage at 4 °C. In fact, both heart polar lipid and *E. coli* lipid HT-AQP2 crystals improved in quality during this period of time, finally becoming indistinguishable in terms of unit cell dimensions, geometry and symmetry. This was rather unexpected, because lipids have often been observed to dictate the crystallization process in terms of order and morphology. Pertinent examples are Bacteriorhodopsin, which requires the native purple membrane lipids,<sup>35</sup> and the porin OmpF, which assembles into different lattice types depending on the nature of the lipid and the LPR used.<sup>36</sup> With

AQP1, polymorphism depending on the LPR and the presence of  $\text{Mg}^{2+}$ ,<sup>37</sup> has been reported. The fact that HT-AQP2 formed identical crystals with two different lipid extracts suggests that co-purified endogenous lipids and/or protein-protein contacts have an important influence on the packing arrangement of the HT-AQP2 arrays, excluding extraneous lipids. This interpretation is compatible with the large lipid areas observed during AFM analyses of these crystals (see below).

#### Characterization of the AQP2 crystals by TEM

Micrographs of negatively stained 2D crystal preparations, optimized as described above, revealed rectangular mono-crystalline arrays of up to 30  $\mu\text{m}$  side length (Figure 1(b)) that diffracted to better than  $15 \text{ \AA}^{-1}$ . Such arrays were highly ordered as demonstrated by electron diffraction of trehalose-embedded HT-AQP2 crystals, which

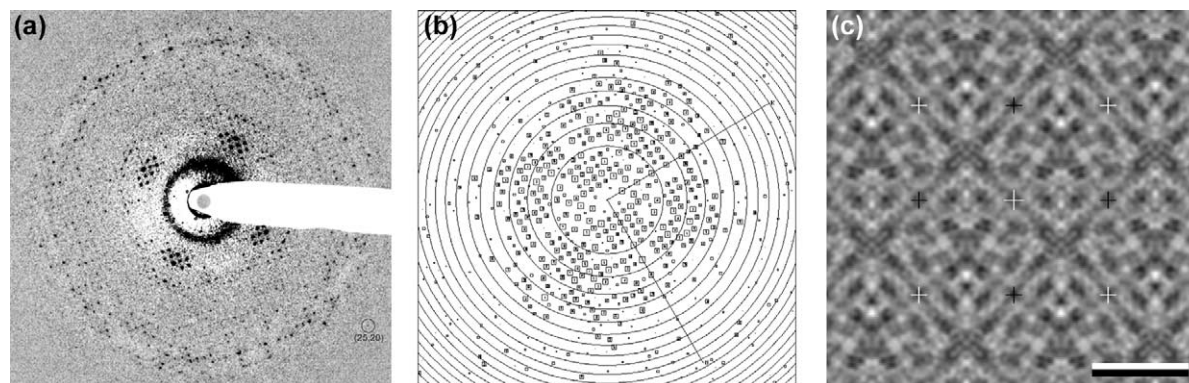


**Figure 2.** Cryo-electron microscopic analysis of 2D AQP2 crystals. (a) Typical electron diffraction pattern of an AQP2 crystal, revealing diffraction up to order (25,20), which corresponds to a resolution of  $3.03 \text{ \AA}^{-1}$ . (b) IQ plot of a cryo electron micrograph of an AQP2 crystal. The IQ plot extends to  $4.66 \text{ \AA}^{-1}$ . (c) Cryo projection map calculated by merging the phase information from ten well preserved AQP2 crystals and the amplitude information from 31 diffraction patterns, and imposing  $p22_12$  symmetry. Scale bar corresponds to 50 Å.

showed orders up to (25,20) (Figure 2(a)), corresponding to a resolution of  $3.03 \text{ \AA}^{-1}$ . Unexpectedly, however, the unit cell projection maps did not reveal the characteristic pattern of AQP tetramers (data not shown). Exploring possible crystallographic packing arrangements by ALLSPACE of the MRC suite, the best symmetry turned out to be  $p22_12$  with a phase residual of  $38^\circ$  considering 460 reflections in total. The map shown in Figure 2(c) was calculated by taking the phases of ten projection maps up to a resolution of  $4.9 \text{ \AA}$  (example given in Figure 2(b)), imposing  $p22_12$  symmetry, and combining them with amplitudes from 31 electron diffraction patterns.

### Mass-per-area determination (MPA)

Mass-per-area (MPA) measurements performed with the scanning transmission electron microscope (STEM<sup>38</sup>) yielded a histogram with several distinct peaks (Figure 3; low mass range only; excluding values from lipid areas). The peaks at  $3.6(\pm 0.2) \text{ kDa/nm}^2$  ( $n=49$ ) and  $6.7(\pm 0.2) \text{ kDa/nm}^2$  ( $n=335$ ) correspond to those observed for AQP0 single and double-layered sheets,<sup>39</sup> with MPAs  $3.4(\pm 0.3) \text{ kDa/nm}^2$  and  $6.6(\pm 0.4) \text{ kDa/nm}^2$ , respectively, and for AqpZ single layer sheets,<sup>34</sup> MPA  $3.2(\pm 0.1) \text{ kDa/nm}^2$ . Mainly as a result of a large glycane and the slightly denser packing, single-layered crystalline sheets of AQP1 have an MPA of  $4.1(\pm 0.3) \text{ kDa/nm}^2$ .<sup>40</sup> Although double-layered 2D crystals were the most predominant form of the HT-AQP2 crystals, stacks thereof and of unfilled lipid bilayers were also found (data not shown).

### Characterization of the AQP2 crystals by AFM

Atomic force topographs recorded from HT-AQP2 2D crystals adsorbed to atomically flat mica

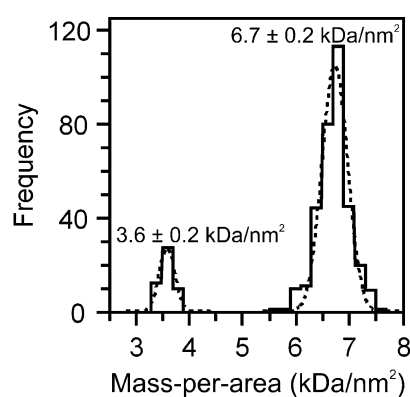


**Figure 3.** STEM mass/area measurements of 2D AQP2 crystals. Mass/area values binned in a histogram were fitted with Gaussian curves. The peak at  $3.6(\pm 0.2) \text{ kDa/nm}^2$  representing single sheets comprises 49 measurements and the peak resulting from double layers at  $6.7(\pm 0.2) \text{ kDa/nm}^2$  is from 335 measurements.

showed 2D crystals with a thickness of  $118(\pm 2) \text{ \AA}$  ( $n=21$ ). Compared to single-layered 2D crystals of AQP1 ( $58(\pm 4) \text{ \AA}$ <sup>41,42</sup>) and single-layered 2D crystals of the bacterial aquaporin AqpZ ( $57(\pm 4) \text{ \AA}$ <sup>43</sup>) this showed that the HT-AQP2 crystals measured were double-layered. While a few single-layers were found during the STEM measurements, no single-layers were detected in the course of the AFM experiments. However, protein-free lipid areas having a thickness of about 4 nm were frequently observed. The same AQP2-surface was always exposed to the AFM stylus, as clearly evident from the high-resolution topographs recorded under optimized buffer conditions using low applied forces<sup>44</sup> (Figure 1(c)). Since no feature of these clean HT-AQP2 topographs had any similarity to the highly corrugated nature of His-tag-bearing AqpZ crystals,<sup>45</sup> the AQP2 surface characterized by AFM is most likely the extracellular one. All of the high-resolution topographs exhibit the same characteristics (averaged in Figure 4(a)). The  $98 \text{ \AA}$  unit cell with  $p4$  symmetry contains two non-crystallographically related but identical AQP2 tetramers, one rotated clockwise by  $45.0(\pm 1.8)$  degrees ( $n=280$ ) around the tetramer's internal 4-fold axis, the other rotated clockwise by  $53.7(\pm 1.5)$  degrees ( $n=247$ ), taking the monomer-monomer interface and lattice vectors for angle-determination. Interestingly, these two tetramers protruded out of the membrane with small, yet significant differences in height:  $16.4(\pm 1.7) \text{ \AA}$  ( $n=280$ ) and  $15.3(\pm 1.9) \text{ \AA}$  ( $n=247$ ), respectively.

The HT-AQP2 topographs resemble those of the extracellular AQP0 surface.<sup>45</sup> The similarity is pronounced in that these proteins lack the prominent protrusions observed around the tetramer's 4-fold axis for AqpZ<sup>43</sup> and AQP1.<sup>46</sup> This is the result of the particularly short A-loop in both AQP2 and AQP0, which is longer in AqpZ and even longer in AQP1.<sup>6</sup> Taken together, these results strongly suggest that HT-AQP2 2D crystals only expose the extra-cellular side of HT-AQP2 to the medium, and that the cytoplasmic N and C termini of HT-AQP2 are trapped within the double-layered sandwich.

### Layer separation

Electron diffraction patterns (Figure 2(a)) of double-layered HT-AQP2 2D crystals showed single lattices, rather than the epitaxial twinned lattices expected from double-layers rotated randomly with respect to each other. Thus, the double-layers were well aligned angularly, although possibly shifted. To determine the shift vector  $\kappa$  between the top and bottom layer in the double-layered HT-AQP2 2D crystals, a synthetic projection map of a single layer was generated based on AFM topographs of HT-AQP2 2D crystals (Figure 4(a)) and the AQP1 PDB model 1H6I (see Materials and Methods). This single layer model shown in Figure 4(b) was used for cross-correlation

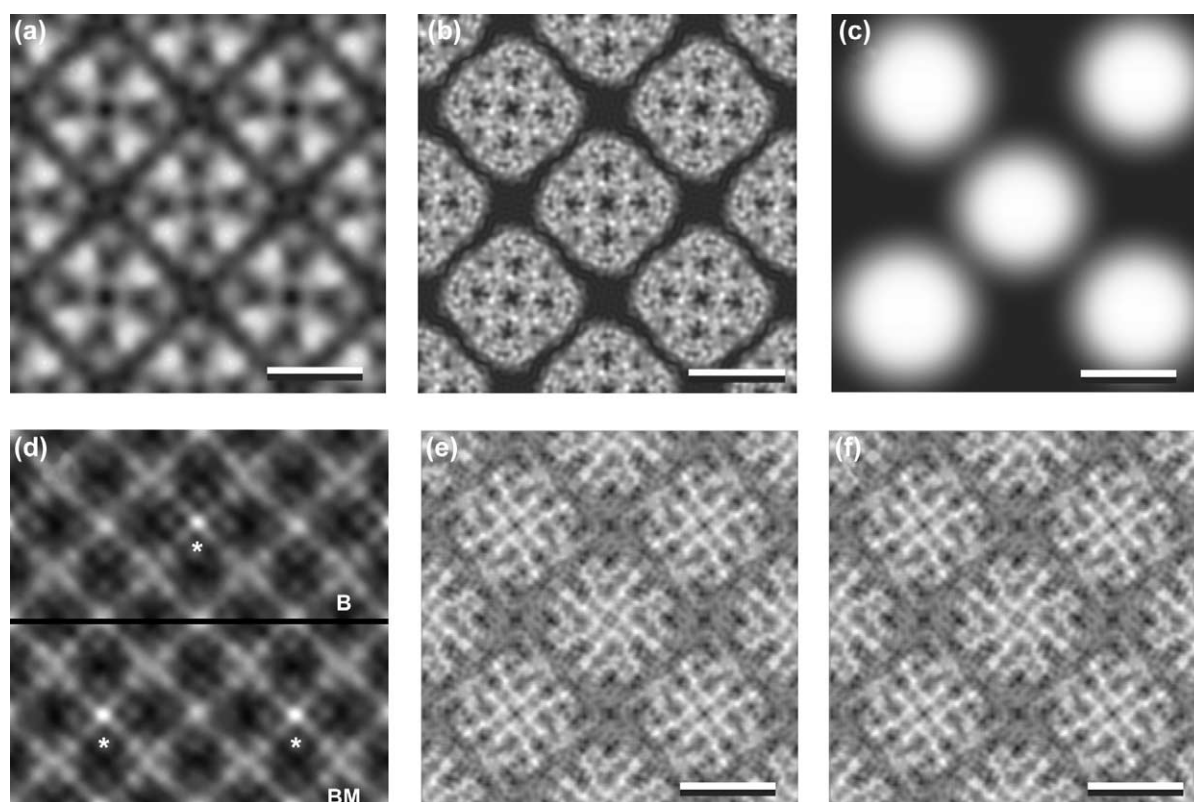


**Figure 4.** Iterative layer separation of 2D AQP2 crystals. (a) Fourier-filtered AFM topograph of an AQP2 crystal, revealing two unique tetramers within the unit cell, rotated by nine degrees with respect to each other. The AQP2 unit cell exhibits  $p4$  symmetry and has a size of 98 Å. (b) Single-layered AQP2 model obtained by projecting the atomic structure of AQP1 along the 4-fold axis and taking the geometrical data from the AFM topograph. (c) Low-resolution AQP2 projection map, as used for iterative layer separation. (d) Cross-correlation between an unsymmetrized AQP2 projection map and either the top layer model shown in (b), (cross-correlation function B), or the bottom layer model (i.e. mirrored top layer; cross-correlation function BM). The highest correlation peaks indicated by asterisks document the shift of half a unit cell between top and bottom layers. (e) Iterative layer separation result using the AQP2 model shown in (b), and (f) using the low-resolution model shown in (c). Results shown are after 1000 cycles. Both starting models converged to very similar single layer projections of AQP2 (differences < 0.2%). For details see Materials and Methods. Scale bars correspond to 50 Å.

with the unsymmetrized AQP2 crystal projection map either directly (to determine the top layer position (Figure 4(d), B)) or after mirroring (to determine the bottom layer position (Figure 4(d), BM)). As indicated by the position of the highest cross-correlation peaks in Figure 4(d), the shift between the two layers of the AQP2 double-layered crystal corresponds to half a unit cell length, i.e.  $\kappa=(0.5,0)$ , resulting in an overall  $p22_12$  symmetry for the double layer.

As demonstrated previously, stacked layers can be deconvoluted to produce single layer projection maps.<sup>47</sup> However, the deconvolution approach cannot be applied to double-layered crystals, whose layers are shifted with respect to each other by an integer fraction (i.e.  $\kappa=1/n, 1/m$ ; with  $n, m$  being integers). In this case systematic absences of diffraction orders implicate division by zero (see Materials and Methods). Because one would expect that for all highly ordered double-layered crystals the shift will be an integer fraction of the unit cell along one or both of the lattice vectors to warrant a

precise, repetitive interaction between the layers, the previously proposed deconvolution method is not useful. Therefore, a novel, iterative real-space algorithm was developed that does not need division, but requires the single layer to have a plane-group symmetry higher than that of the double layer, which can be revealed by various techniques, e.g. by AFM (see Materials and Methods).

When the single layer model calculated from the AQP1 structure was used as the initial model (Figure 4(b)), the algorithm produced a projection map typical of single-layered aquaporin crystals (Figure 4(e)). The iteration process converged rapidly since the contribution of the shifted, second layer was reduced by 1/4 for each cycle, whereas that of the first layer centered about the 4-fold axis was not attenuated. The rotation angles of the two unique tetramers in this map, 45° and 54°, compare favorably to those determined by AFM. A single layer projection map that was virtually identical to the one calculated with the AQP1-based starting

**Table 2.** Electron crystallographic data

Plane group symmetry	$P222_1$
Unit cell	$a = b = 98 \text{ \AA}$ ; $c = 140 \text{ \AA}$ (assumed) $\alpha = \beta = \gamma = 90^\circ$
Number of processed images	363 ( $0^\circ:69$ $15^\circ:115$ $20^\circ:6$ $30^\circ:23$ $45^\circ:150$ )
Number of merged phases	22,068
Resolution limit for merging	4.5 Å (in the membrane plane; $x,y$ -direction) 6.67 Å (perpendicular to the membrane plane; $z$ -direction)
Phase residual (IQ-weighted) <sup>a</sup>	37.1° (Overall) 26.9° (100–9.7 Å) 33.2° (9.7–6.9 Å) 67.8° (6.9–5.6 Å) 85.7° (5.6–4.9 Å) 86.5° (4.9–4.5 Å)
Completeness <sup>b</sup>	20% (resolution volume: 4.5 Å) 60% (resolution volume 6.67 Å)

<sup>a</sup> Determined by AVRAMPHS (MRC program suite).  
<sup>b</sup> Determined by SFCHECK (CCP4), the missing cone is included in this volume.

model was obtained even when a coarse initial single layer model, e.g. circular blobs representing the HT-AQP2 tetramers (Figure 4(c)), was used (compare Figure 4(e) with (f)). Indeed, any coarse single layer starting model, such as the topograph acquired by AFM, produced a map similar to those shown in Figure 4(e) and (f), provided that the values of order ( $h, k$ ) that vanish in the transform of the double layer projection map are also small in the starting model. Therefore, the algorithm developed resets such orders to 0 in each cycle of the iteration. This resulted in a robust and efficient layer separation method that is generally applicable, provided that the plane-group symmetry of the single layer and the shift vector are known.

The resolution of the reconstructed single layer projection map was determined by Fourier ring correlation analysis,<sup>48</sup> comparing the two non-crystallographically related tetramers. A resolution of 4.9 Å was obtained using the 0.5 criterion. Since the number of orders carrying structural infor-

mation increases with the square of the resolution, but the number of systematic absences only linearly, the completeness of information is close to 97% at a resolution of  $3 \text{ \AA}^{-1}$  and still about 95% at  $5 \text{ \AA}^{-1}$  for the AQP2 lattices described here.

### 3D potential map

The information on the architecture of the double-layered crystals allowed projection maps of tilted samples to be interpreted, and the phase origins of projections recorded at lower tilt angles ( $10$ – $20^\circ$ ) to be determined. An initial 3D map thus reconstructed made it possible to subsequently determine the phase origins of projections recorded at higher tilt angles ( $30$ – $45^\circ$ ), and to merge the data set. In total the information was extracted from 363 images, of which 150 images were recorded at a tilt angle of  $45^\circ$  (Table 2). Image shift due to beam-induced specimen charging was a major problem when recording images at tilt angles above  $30^\circ$ .

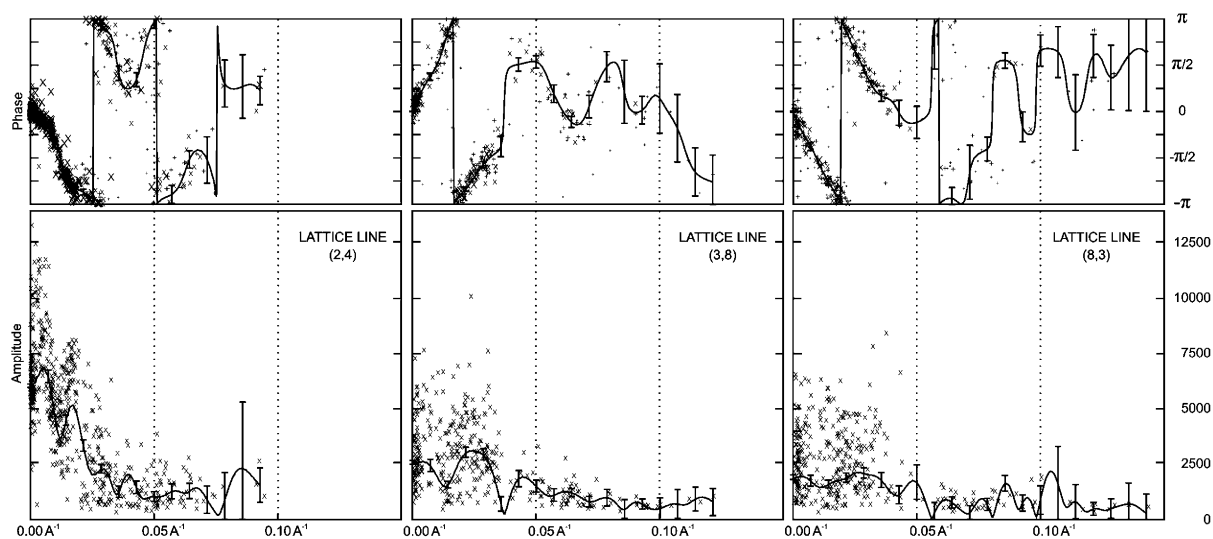


**Figure 5.** Lattice lines. Amplitude-phase pairs were extracted from 363 projection maps calculated from micrographs recorded over a tilt angle range of  $0^\circ$  to  $45^\circ$ .

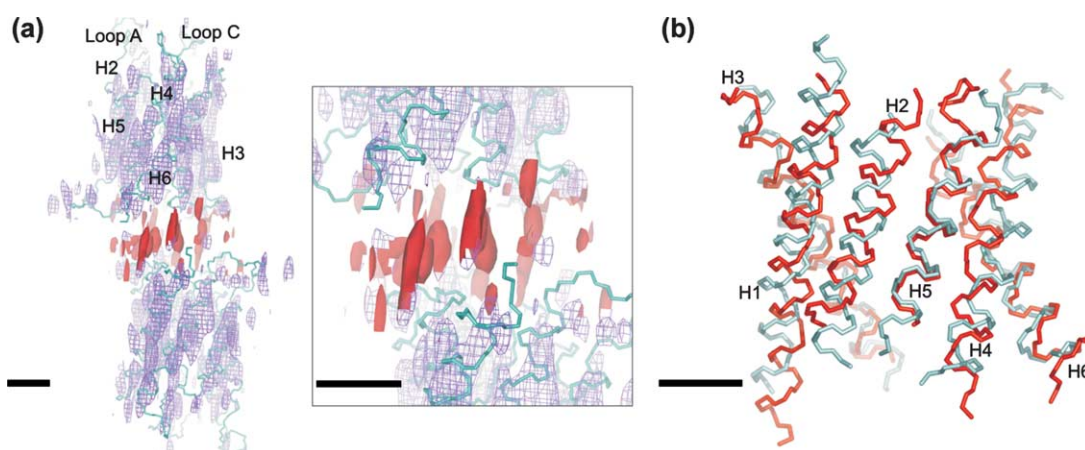


**Figure 6.** 3D potential map. (a) Two AQP2 monomers are shown in purple, one from the top layer, the other from the bottom layer. The fitted alpha-carbon backbone of AQP1 is displayed in cyan. The putative density of the termini is indicated in red. The inset provides a closer look at the termini section. (b) The helical fragments fitted to the map shown in (a) are colored in red and overlaid on the AQP1 helices in cyan. Scale bars represent 10 Å.

Attempts to overcome this difficulty included (i) the spot-scan mode,<sup>49</sup> (ii) evaporating a second carbon film onto glucose-embedded, air-dried samples,<sup>50</sup> and (iii) deposition of a second carbon film on the wet sample before freezing.<sup>51</sup> Each method has its own limitations. The first increases the difficulties in image processing, mainly in the lattice unbending procedure. The second method gave the most reproducible improvements, but can induce dehydration collapse if there is not sufficient support by the glucose. The third method is in theory the best, but it is experimentally the most difficult. Therefore, the quality of images recorded at 60° tilt was inferior to that of images acquired at 45°, explaining the lack of 60° projection data in our current data set.

Some of the lattice line data are shown in Figure 5. They demonstrate the quality of the phase information along  $z^*$  up to a resolution of 10 Å, while the amplitude data exhibit a significant scatter. The resolution range between 10 and 7 Å is sparsely populated, but still carries significant information. The 3D potential map calculated from this data set is displayed in Figure 6, showing two monomers, one from the upper layer and the other from the lower layer. The double layer has a thickness of 117 Å, compatible with the value acquired by AFM (118(±2) Å).

When the alpha-carbon backbone of AQP1 was fitted to the AQP2 3D map an intermediate layer of densities became visible, which could not be explained by any features of the AQP1 structures available. These structures do not provide information about the last 36 (hAQP1; 1H6I<sup>9</sup>) or 22 (bAQP1; 1J4N<sup>11</sup>) C-terminal residues. The major difference between the structure of AQP1 and that of AQP2 presented here is therefore most likely the result of contributions from the N and C termini, which appear to dictate the packing arrangement of the double-layered 2D crystals.

To further explore differences between AQP1 and

AQP2, the program ROTTRANS<sup>52</sup> was used to fit helical segments to the 3D potential map of AQP2. Although the resolution along  $z^*$  did not suffice to identify the direction of the helices, the fitted segments allowed the tilt angles of transmembrane helices to be determined. The helices of AQP2 exhibit tilt angles with respect to the  $z$ -axis that are rather close to those of AQP1. However, the differences in angles between respective helices range from a few degrees up to more than ten degrees: H1 (2.0°); H2 (9.1°); H3 (5.1°); H4 (4.6°); H5 (10.8°) and H6 (6.0°). The largest differences are found in H2 and H5, which are the shortest of the six transmembrane helices.

## Conclusion

The double-layered 2D crystals of HT-AQP2 described here are highly ordered and provides a solid basis to assess the atomic structure of this medically important aquaporin. Although it is challenging to establish the 3D structure of double-layered 2D crystals they appear to be better ordered to start with, and to be more stable than single layered crystals. Single layer HT-AQP2 projection maps calculated by a novel, iterative algorithm using different starting models exhibit all the features expected for an aquaporin projection map at 4.9 Å resolution. This documents the usefulness of the layer separation algorithm introduced for processing projection maps of double-layered 2D crystals. The overall features of the AQP2 monomer resemble those of AQP1. However, a striking new feature is the layer of densities sandwiched between the two single-layered crystal sheets, which we attribute to the N and C termini. Although the vertical resolution of this map (7 Å) does not suffice to resolve these possibly intertwined but highly ordered termini, electron

diffraction at high tilt angles is expected to unravel their structure. The current study represents a first step towards this goal and shows the potential of the 2D crystals produced.

## Materials and Methods

### Expression and purification of AQP2

Human AQP2 was recombinantly expressed as an N-terminally His-tagged protein (HT-AQP2) in the baculovirus/insect cell expression system, and purified as described earlier<sup>32</sup> with some minor modifications. Briefly, Sf9 cells were grown to a density of  $1.5 \times 10^6$  cells/ml in a 15 liter Bioreactor (Applikon) containing ten liters of Insect Xpress medium (BioWhittaker). Cells were infected with HT-AQP2 encoding baculovirus at a multiplicity of infection (MOI) of 0.05. Five days after infection, they were harvested by ten minutes centrifugation at 5000g and 4 °C, and homogenized in ice-cold 5 mM Tris-HCl (pH 8.0), 100 mM NaCl by 20 strokes at 500 rpm in Potter-Elvehjem tubes, followed by 20 strokes of douncing. An equivalent of  $1 \times 10^8$  cells/ml was used throughout the entire stripping and solubilization procedure. Crude membranes were pelleted by 30 minutes centrifugation at 100,000g and 4 °C. This membrane pellet was homogenized in 5 mM Tris (pH 8.0), 1 mM EDTA, 4 M urea as above, and centrifuged for 45 minutes at 100,000g and 4 °C. The resulting pellet was homogenized in 20 mM NaOH (pH 12) and centrifuged for 90 minutes at 100,000g and 4 °C. This pellet was subjected to two rounds of homogenization in 5 mM Tris (pH 8.0), 100 mM NaCl and 30 minutes centrifugation at 100,000g and 4 °C, to restore the pH. The final stripped pellet was homogenized in solubilization buffer (20 mM Tris (pH 8.0), 300 mM NaCl, 1 mM L-histidine, 0.01% (w/v) NaN<sub>3</sub>) containing 4% *n*-octyl- $\beta$ -D-glucopyranoside (OG), by 20 strokes at 500 rpm in Potter-Elvehjem tubes, and solubilized by stirring gently for two hours at 4 °C. Solubilized proteins were separated from insoluble material by 60 minutes centrifugation at 100,000g and 4 °C, and diluted by the addition of an equal volume of solubilization buffer. Ni-NTA beads were added to the solubilized proteins (15  $\mu$ l of Ni-NTA beads per equivalent of  $1 \times 10^8$  cells) and gently stirred at 4 °C for four hours. The Ni-NTA beads were then centrifuged for 15 minutes at 4000g and 4 °C, washed once with solubilization buffer containing 2% OG, and packed onto spin columns (Promega, A7651) by gravity flow. After 45 minutes incubation of the columns with elution buffer (solubilization buffer containing 2% OG and 100 mM L-histidine; 30  $\mu$ l per equivalent of  $1 \times 10^8$  cells), pure HT-AQP2 was eluted by two minutes centrifugation at 2000 rpm in an Eppendorf centrifuge, and directly used for crystallization.

### Crystallization of AQP2

Lipid stocks (Avanti Polar Lipids) were solubilized in 2% OG at a concentration of 3 mg/ml and mixed with freshly prepared HT-AQP2 for crystallization trials. Initial trials were conducted in dialysis buttons with a volume of 60  $\mu$ l, covered with a 10 kDa-cutoff dialysis membrane and dialyzed by submerging in 11 flasks with the respective dialysis buffer. Final optimizations of the crystallization conditions were performed in 100  $\mu$ l volumes in a temperature-controlled dialysis machine,<sup>33</sup> using the following profile: 12 hours at 20 °C, 24 hours

linear ramp to 37 °C, 24 hours at 37 °C, 12 hours linear ramp to 20 °C. A summary of the conditions tested is given in Table 1.

### Scanning transmission electron microscopy

For mass measurement, 7  $\mu$ l aliquots of the HT-AQP2 samples were adsorbed for 45 s to glow discharged thin carbon films that spanned a thick fenestrated carbon layer covering 200-mesh/inch, gold-plated copper grids. The grids were blotted, washed on four drops of quartz bi-distilled water and freeze-dried overnight in the microscope at  $-80^\circ\text{C}$  and  $5 \times 10^{-8}$  Torr. To calibrate the instrument, tobacco mosaic virus particles (kindly supplied by Dr R. Diaz-Avalos, Institute of Molecular Biophysics, Florida State University) were similarly adsorbed to a separate grid and air-dried.

Dark-field images were recorded from the unstained samples using a Vacuum Generators STEM HB-5 interfaced to a modular computer system (Tietz Video and Image Processing Systems GmbH, D-8035 Gauting). The accelerating voltage was 80 kV. A nominal magnification of  $200,000\times$  and recording doses in the range of 350 electrons/nm<sup>2</sup> were employed. Details of the instrument's calibration for mass measurement may be found in the publication by Müller *et al.*<sup>38</sup>

The  $512 \times 512$  pixel digital images were evaluated using the program package IMPSYS as described.<sup>38</sup> Accordingly, sheet areas were defined by circular boxes and the total scattering of each calculated. The average background scattering of empty carbon support film adjacent to the sheets was subtracted and the MPA of the 2D crystals calculated. The resulting values were corrected for beam-induced mass-loss based on the behavior of 2D AqpZ crystals.<sup>34</sup> The mass data were displayed in histograms and fitted by Gauss curves.

### Atomic force microscopy

A stock solution of 2D HT-AQP2 crystals (0.7 mg/ml protein) was diluted 30-fold in imaging buffer (20 mM Tris (pH 7.8), 150 mM KCl, 25 mM MgCl<sub>2</sub>) and adsorbed for 20–30 minutes to freshly cleaved muscovite mica. After adsorption, the sample was gently washed with imaging buffer to remove membranes that were not firmly attached to the substrate. AFM experiments were performed using a Nanoscope III AFM (Digital Instruments, Veeco Metrology Group, Santa Barbara, CA, USA) equipped with a 150  $\mu$ m J-Scanner, a fluid cell, and oxide-sharpened silicon nitride cantilevers of 100  $\mu$ m length, with nominal spring constants of 0.09 N/m (Olympus Optical Co. and Digital Instruments, respectively). Topographs were acquired in contact mode at minimal loading forces (<100 pN).<sup>44</sup> Trace and retrace signals were recorded simultaneously at line frequencies ranging between 4.1 and 5.1 Hz.

### Transmission electron microscopy

For imaging of negatively stained HT-AQP2 crystals, the protein sample was adsorbed for 5 s to glow-discharged, carbon film-coated copper grids and subsequently stained with 0.75% uranyl formate. Images were recorded on Kodak SO-163 film on a Hitachi H8000 TEM, at 100 kV and a nominal magnification of  $50,000\times$ .

Cryo-electron microscopy images and diffraction patterns were recorded from unstained samples, using a Philips CM200FEG TEM equipped with a Gatan cryo

stage. Molybdenum grids (a kind gift from Dr Y. Fujiyoshi) coated with carbon films were prepared by the back-injection technique<sup>53</sup> using 2% (w/v) trehalose as embedding medium. Sample grids were frozen in liquid nitrogen and transferred to a Gatan cryo holder. Alternatively, samples were prepared in 2% (w/v) glucose and dried before cooling in the cryo holder. Diffraction patterns were recorded at 95 K, 200 kV, and a camera length of 1 m, using a Gatan UltraScan™ 2k×2k CCD camera. Images were recorded on Kodak SO-163 film at 200 kV and a nominal magnification of 50,000×, keeping the sample at 95 K. Attempts to overcome film charging included the spot scan mode,<sup>49</sup> evaporating a carbon layer onto the dried crystals,<sup>50</sup> or depositing a second carbon film onto the wet sample.<sup>51</sup>

### Image processing

Electron micrographs were digitized with a Heidelberg Primescan D 7100 at 1 Å/pixel at the specimen level. Images and diffraction patterns recorded by cryo-EM were processed using the MRC software package.<sup>54–56</sup> Images were unbent three times, using Fourier-filtered versions of the respective images as a reference. Indexing of images was performed automatically using the SPIDER software package<sup>57</sup> to perform a peak search and a self-written program to determine the crystal lattice. The crystal symmetry was determined by the MRC program ALLSPACE. Electron diffraction patterns were corrected for background arising from inelastically scattered electrons and indexed using the MRC programs BACKAUTO and AUTOINDEX. Integration of the diffraction spots was carried out using the program PICKAUTO of the MRC package. A self-written program that calculates and applies scale factors to the diffraction data before combining the two datasets performed merging of diffraction amplitudes with image amplitudes and phases.

### Layer separation

For the case of a double layer projection normal to the plane of the membrane the Fourier transform  $G_d(h,k)$  can be written as:

$$G_d(h,k) = G_b(h,k) + G_t(h,k)\{\exp(-2\pi i \xi h)\} \quad (1)$$

where  $G_b(h,k)$  and  $G_t(h,k)$  represent the transforms of the bottom and the top layer,  $h,k$  the indices of the diffraction order, and  $\xi$  is the shift along the  $x$ -axis in fractions of the unit cell length. If layers are stacked unidirectionally, the transform of the single layer is obtained by deconvolution:

$$G_b(h,k) = G_t(h,k) = G_d(h,k)/(1 + \{\exp(-2\pi i \xi h)\}) \quad (2)$$

As a result of systematic absences for orders  $(\pm 2n+1, k)$ , deconvolution cannot be applied when the shift  $\xi=0.5$  or generally  $1/n$  with  $n$  being an integer. For double layers that are stacked face-to-face by rotation of one layer by  $\pi$  around the  $y$ -axis, the transforms of the single layer projections are related by:

$$G_b(h,k) = G_t(-h,k) \quad (3)$$

For single layers lacking mirror symmetry, identities  $G_b(h,k)=G_t(h,k)$  are found for orders  $(\pm n,0)$  if the single layers exhibit  $p2$  symmetry, and additionally for orders  $(0,\pm n)$  and  $(\pm n,\pm n)$  if the single layers have  $p4$  symmetry. Systematic absences thus occur for orders  $h,k = \pm 2n+1, 0$  ( $p2$ ), and additionally for diagonal orders

$h=k = \pm 2n+1$  ( $p4$ ) if double layers are shifted with respect to each other by half a unit cell along the  $x$ -axis, again preventing the application of the separation specified by equation (2). Therefore, a real-space iteration method was used to generate a single layer projection map from the double-layered HT-AQP2 crystals. To determine the shift between the two layers, the *iplt* image processing software tools<sup>58</sup> were used to cross-correlate the double layer projection map with a single layer model and its mirror image. The shift vector  $\kappa$  was obtained from the position of the cross-correlation maxima. The single layer model was constructed using a combination of geometry information from AFM topographs of HT-AQP2 crystals and the calculated electron density map of tetramers built from the AQP1 PDB file 1H6I.<sup>9</sup> The software SEMPER<sup>59</sup> was used to determine the position and rotational angle of the individual tetramers in the HT-AQP2 unit cell derived from AFM topographs, and programs from the GROMACS package† were used to build the AQP1 tetramers. The projection map of the single layer model was generated with the CCP4 suite‡.<sup>60</sup>

A high-resolution single layer projection map was then obtained by a real-space iteration algorithm, implemented as an *iplt* script. This iteration was carried out with different starting models to test the robustness of the method: (i) with the AQP1 single layer model (described above), (ii) with an artificial model (simple blobs representing the AQP2 tetramers), (iii) with random noise, and (iv) with the topograph acquired by AFM. In each case, the reference was scaled such that the half peak width of its intensity distribution equaled one times that of the double layer. Subtraction of the single layer model from the double layer yielded a new single layer model. This new single layer model, now carrying more information from the AQP2 projection map, was mirrored, shifted by  $\kappa$  and 4-fold symmetrized. To improve the robustness of the method, reflections that were systematically absent in the Fourier transform of the double layer were also set to zero in the single layer model. The new model was averaged with the model from the previous cycle, scaled and subtracted from the double layer. This procedure was repeated until the result converged.

### Calculation of the 3D potential map

The tilt geometry of the micrographs was determined by measuring the defocus by CTF-fitting in  $7 \times 7$  sub-areas of the image and then fitting a least squares plane through the 49 points. For the projections recorded at low tilt angle the phase origins were first determined by eye. Then the images were merged and scaled using the program ORIGIN and lattice line curves were fitted with LATLINE, both of the MRC program suite. The obtained dataset then served as reference for finding the phase origin and scaling factor of the projections taken at higher tilt angles. In a cyclical refinement procedure the tilt geometry, beam tilt, phase origin and scaling factor were improved to obtain a more accurate potential map. At the start of each cycle, every individual image was compared with the fitted dataset using ORIGIN to determine new values for the image parameters mentioned above. For the next cycle, all images were merged using the new

† <http://www.gromacs.org>

‡ <http://www.ccp4.ac.uk>

image parameters and the LATLINE program was used to generate a new reference data set.

### Helix-fitting

Helical fragments were fitted to the 3D potential map of AQP2 as described.<sup>52</sup> The program ROTTRANS (obtainable free†) was used for full rotation and translation searches through the AQP2 3D map. A set of 38  $\alpha$ -helical fragments was extracted from the Protein Data Bank, mutated to poly-valine helices, and taken as probe helices for ROTTRANS. Positions and tilt angles of the six transmembrane helices were then derived from the fitted helical segments and compared to the same parameters calculated for AQP1.

### Acknowledgements

We thank Dr Y. Fujiyoshi for a kind gift of Molybdenum grids, Dr R. Henderson for providing a copy of the CONVDECONV program, Dr R. Diaz-Avalos for the tobacco mosaic virus particles and Vesna Olivieri for the STEM microscopy. We are thankful to Dr Peter Dean for his strong support in the early phase of the project and to Dr Wim de Grip for his help with the large-scale expression of AQP2. This work was supported by the Swiss National Science Foundation (grant number NF31-59415.99) to A.E., the M.E. Müller foundation of Switzerland, the National Center of Competence in Research (NCCR) for Structural Biology, and the EC-CONTRACT QLK3-1999-00778.

### References

- Agre, P. & Kozono, D. (2003). Aquaporin water channels: molecular mechanisms for human diseases. *FEBS Letters*, **555**, 72–78.
- Agre, P., King, L. S., Yasui, M., Guggino, W. B., Ottersen, O. P., Fujiyoshi, Y. *et al.* (2002). Aquaporin water channels—from atomic structure to clinical medicine. *J. Physiol.* **542**, 3–16.
- King, L. S., Yasui, M. & Agre, P. (2000). Aquaporins in health and disease. *Mol. Med. Today*, **6**, 60–65.
- Deen, P. M. T. & van Os, C. H. (1998). Epithelial aquaporins. *Curr. Opin. Cell Biol.* **10**, 435–442.
- Engel, A., Fujiyoshi, Y. & Agre, P. (2000). The importance of aquaporin water channel protein structures. *EMBO J.* **19**, 800–806.
- Heymann, J. B. & Engel, A. (2000). Structural clues in the sequences of the aquaporins. *J. Mol. Biol.* **295**, 1039–1053.
- Jung, J., Preston, G., Smith, B., Guggino, W. & Agre, P. (1994). Molecular structure of the water channel through aquaporin CHIP. The hourglass model. *J. Biol. Chem.* **269**, 14648–14654.
- Murata, K., Mitsuoka, K., Hirai, T., Walz, T., Agre, P., Heymann, J. B. *et al.* (2000). Structural determinants of water permeation through aquaporin-1. *Nature*, **407**, 599–605.
- de Groot, B. L., Engel, A. & Grubmüller, H. (2001). A refined structure of human aquaporin-1. *FEBS Letters*, **504**, 206–211.
- Ren, G., Reddy, V. S., Cheng, A., Melnyk, P. & Mitra, A. K. (2001). Visualization of a water-selective pore by electron crystallography in vitreous ice. *Proc. Natl Acad. Sci. USA*, **98**, 1398–1403.
- Sui, H., Han, B. G., Lee, J. K., Walian, P. & Jap, B. K. (2001). Structural basis of water-specific transport through the AQP1 water channel. *Nature*, **414**, 872–878.
- Gonen, T., Sliz, P., Kistler, J., Cheng, Y. & Walz, T. (2004). Aquaporin-0 membrane junctions reveal the structure of a closed water pore. *Nature*, **429**, 193–197.
- Harries, W. E., Akhavan, D., Miercke, L. J., Khademi, S. & Stroud, R. M. (2004). The channel architecture of aquaporin 0 at a 2.2-Å resolution. *Proc. Natl Acad. Sci. USA*, **101**, 14045–14050.
- Fu, D., Libson, A., Miercke, L. J., Weitzman, C., Nollert, P., Krucinski, J. & Stroud, R. M. (2000). Structure of a glycerol-conducting channel and the basis for its selectivity. *Science*, **290**, 481–486.
- Tajkhorshid, E., Nollert, P., Jensen, M. O., Miercke, L. J., O'Connell, J., Stroud, R. M. & Schulten, K. (2002). Control of the selectivity of the aquaporin water channel family by global orientational tuning. *Science*, **296**, 525–530.
- Savage, D. F., Egea, P. F., Robles-Colmenares, Y., Iii, J. D. & Stroud, R. M. (2003). Architecture and selectivity in aquaporins: 2.5 Å X-ray structure of aquaporin Z. *PLoS Biol.* **1**, E72.
- Nielsen, S., Frokiaer, J. & Knepper, M. A. (1998). Renal aquaporins: key roles in water balance and water balance disorders. *Curr. Opin. Nephrol. Hypertens.* **7**, 509–516.
- Knepper, M. A., Verbalis, J. G. & Nielsen, S. (1997). Role of aquaporins in water balance disorders. *Curr. Opin. Nephrol. Hypertens.* **6**, 367–371.
- Deen, P. M. T. & Knoers, N. V. A. M. (1998). Physiology and pathophysiology of the aquaporin-2 water channel. *Curr. Opin. Nephrol. Hypertens.* **7**, 37–42.
- van Os, C. H. & Deen, P. M. T. (1998). Role of aquaporins in renal water handling: physiology and pathophysiology. *Nephrol. Dial. Transplant.* **13**, 1645–1651.
- Mulders, S. M., Bichet, D. G., Rijss, J. P., Kamsteeg, E. J., Arthus, M. F., Lonergan, M. *et al.* (1998). An aquaporin-2 water channel mutant which causes autosomal dominant nephrogenic diabetes insipidus is retained in the Golgi complex. *J. Clin. Invest.* **102**, 57–66.
- Deen, P. M. T., Verdijk, M. A. J., Knoers, N. V. A. M., Wieringa, B., Monnens, L. A. H., van Os, C. H. & van Oost, B. A. (1994). Requirement of human renal water channel aquaporin-2 for vasopressin-dependent concentration of urine. *Science*, **264**, 92–95.
- Nielsen, S., Kwon, T. H., Christensen, B. M., Promeneur, D., Frokiaer, J. & Marples, D. (1999). Physiology and pathophysiology of renal aquaporins. *J. Am. Soc. Nephrol.* **10**, 647–663.
- Xu, L., Poole, D. C. & Musch, T. I. (1998). Effect of heart failure on muscle capillary geometry: implications for O<sub>2</sub> exchange. *Med. Sci. Sports Exerc.* **30**, 1230–1237.
- Nielsen, S., Terris, J., Andersen, D., Ecelbarger, C.,

† [http://www.mpibpc.mpg.de/groups/de\\_groot/bgroot/maptools.html](http://www.mpibpc.mpg.de/groups/de_groot/bgroot/maptools.html)

- Frokiær, J., Jonassen, T. *et al.* (1997). Congestive heart failure in rats is associated with increased expression and targeting of aquaporin-2 water channel in collecting duct. *Proc. Natl Acad. Sci. USA*, **94**, 5450–5455.
26. Schrier, R. W., Fassett, R. G., Ohara, M. & Martin, P. Y. (1998). Vasopressin release, water channels, and vasopressin antagonism in cardiac failure, cirrhosis, and pregnancy. *Proc. Assoc. Am. Physicians*, **110**, 407–411.
27. Jonassen, T. E., Nielsen, S., Christensen, S. & Petersen, J. S. (1998). Decreased vasopressin-mediated renal water reabsorption in rats with compensated liver cirrhosis. *Am. J. Physiol.* **275**, F216–F225.
28. Asahina, Y., Izumi, N., Enomoto, N., Sasaki, S., Fushimi, K., Marumo, F. & Sato, C. (1995). Increased gene expression of water channel in cirrhotic rat kidneys. *Hepatology*, **21**, 169–173.
29. Fernandez-Llama, P., Turner, R., Dibona, G. & Knepper, M. A. (1999). Renal expression of aquaporins in liver cirrhosis induced by chronic common bile duct ligation in rats. *J. Am. Soc. Nephrol.* **10**, 1950–1957.
30. Pearson, J. F. (1992). Fluid balance in severe pre-eclampsia. *Br. J. Hosp. Med.* **48**, 47–51.
31. Schrier, R. W., Ohara, M., Rogachev, B., Xu, L. & Knotek, M. (1998). Aquaporin-2 water channels and vasopressin antagonists in edematous disorders. *Mol. Genet. Metab.* **65**, 255–263.
32. Werten, P. J. L., Hasler, L., Koenderink, J. B., Klaassen, C. H. W., de Grip, W. J., Engel, A. & Deen, P. M. T. (2001). Large-scale purification of functional recombinant human aquaporin-2. *FEBS Letters*, **504**, 200–205.
33. Jap, B. K., Zulauf, M., Scheybani, T., Hefti, A., Baumeister, W., Aebi, U. & Engel, A. (1992). 2D crystallization: from art to science. *Ultramicroscopy*, **46**, 45–84.
34. Ringler, P., Borgnia, M. J., Stahlberg, H., Maloney, P. C., Agre, P. & Engel, A. (1999). Structure of the water channel AqpZ from *Escherichia coli* revealed by electron crystallography. *J. Mol. Biol.* **291**, 1181–1190.
35. Mitra, A. K., Miercke, L. J., Turner, G. J., Shand, R. F., Betlach, M. C. & Stroud, R. M. (1993). Two-dimensional crystallization of *Escherichia coli*-expressed bacteriorhodopsin and its D96N variant: high resolution structural studies in projection. *Biophys. J.* **65**, 1295–1306.
36. Engel, A., Hoenger, A., Hefti, A., Henn, C., Ford, R. C., Kistler, J. & Zulauf, M. (1992). Assembly of 2-D membrane protein crystals: dynamics, crystal order, and fidelity of structure analysis by electron microscopy. *J. Struct. Biol.* **109**, 219–234.
37. Ren, G., Cheng, A., Melnyk, P. & Mitra, A. K. (2000). Polymorphism in the packing of aquaporin-1 tetramers in 2-D crystals. *J. Struct. Biol.* **130**, 45–53.
38. Müller, S. A., Goldie, K. N., Burki, R., Haring, R. & Engel, A. (1992). Factors influencing the precision of quantitative scanning transmission electron microscopy. *Ultramicroscopy*, **46**, 317–334.
39. Hasler, L., Walz, T., Tittmann, P., Gross, H., Kistler, J. & Engel, A. (1998). Purified lens major intrinsic protein (MIP) forms highly ordered tetragonal two-dimensional arrays by reconstitution. *J. Mol. Biol.* **279**, 855–864.
40. Walz, T., Smith, B. L., Zeidel, M. L., Engel, A. & Agre, P. (1994). Biologically active 2-dimensional crystals of aquaporin CHIP. *J. Biol. Chem.* **269**, 1583–1586.
41. Walz, T., Tittmann, P., Fuchs, K. H., Müller, D. J., Smith, B. L., Agre, P. *et al.* (1996). Surface topographies at subnanometer-resolution reveal asymmetry and sidedness of aquaporin-1. *J. Mol. Biol.* **264**, 907–918.
42. Müller, D. J. & Engel, A. (1997). The height of biomolecules measured with the atomic force microscope depends on electrostatic interactions. *Biophys. J.* **73**, 1633–1644.
43. Scheuring, S., Ringler, P., Borgnia, M., Stahlberg, H., Müller, D. J., Agre, P. & Engel, A. (1999). High resolution AFM topographs of the *Escherichia coli* water channel aquaporin Z. *EMBO J.* **18**, 4981–4987.
44. Müller, D. J., Fotiadis, D., Scheuring, S., Müller, S. A. & Engel, A. (1999). Electrostatically balanced subnanometer imaging of biological specimens by atomic force microscope. *Biophys. J.* **76**, 1101–1111.
45. Fotiadis, D., Hasler, L., Müller, D. J., Stahlberg, H., Kistler, J. & Engel, A. (2000). Surface tongue-and-groove contours on lens MIP facilitate cell-to-cell adherence. *J. Mol. Biol.* **300**, 779–789.
46. Fotiadis, D., Suda, K., Tittmann, P., Jenö, P., Philippsen, A., Müller, D. J. *et al.* (2002). Identification and structure of a putative Ca<sup>2+</sup>-binding domain at the C terminus of AQP1. *J. Mol. Biol.* **318**, 1381–1394.
47. Kunji, E. R., Spudich, E. N., Grishammer, R., Henderson, R. & Spudich, J. L. (2001). Electron crystallographic analysis of two-dimensional crystals of sensory rhodopsin II: a 6.9 Å projection structure. *J. Mol. Biol.* **308**, 279–293.
48. Saxton, W. O. & Baumeister, W. (1982). The correlation averaging of a regularly arranged bacterial cell envelope protein. *J. Microsc.* **127**, 127–138.
49. Downing, K. H. (1991). Spot-scan imaging in transmission electron microscopy. *Science*, **251**, 53–59.
50. Brink, J., Gross, H., Tittmann, P., Sherman, M. B. & Chiu, W. (1998). Reduction of charging in protein electron cryomicroscopy. *J. Microsc.* **191**, 67–73.
51. Gyobu, N., Tani, K., Hiroaki, Y., Kamegawa, A., Mitsuoka, K. & Fujiyoshi, Y. (2004). Improved specimen preparation for cryo-electron microscopy using a symmetric carbon sandwich technique. *J. Struct. Biol.* **146**, 325–333.
52. de Groot, B. L., Heymann, J. B., Engel, A., Mitsuoka, K., Fujiyoshi, Y. & Grubmüller, H. (2000). The fold of human aquaporin 1. *J. Mol. Biol.* **300**, 987–994.
53. Hirai, T., Murata, K., Mitsuoka, K., Kimura, Y. & Fujiyoshi, Y. (1999). Trehalose embedding technique for high-resolution electron crystallography: application to structural study on bacteriorhodopsin. *J. Electron Microsc. (Tokyo)*, **48**, 653–658.
54. Henderson, R., Baldwin, J. M., Ceska, T. A., Zemlin, F., Beckmann, E. & Downing, K. H. (1990). Model for the structure of bacteriorhodopsin based on high-resolution electron cryo-microscopy. *J. Mol. Biol.* **213**, 899–929.
55. Henderson, R., Baldwin, J. M., Downing, K. H., Lepault, J. & Zemlin, F. (1986). Structure of purple membrane from halobacterium halobium: recording measurement and evaluation of electron micrographs at 3.5 Å resolution. *Ultramicroscopy*, **19**, 147–178.
56. Baldwin, J. M. & Henderson, R. (1984). Measurement and evaluation of electron diffraction patterns from two-dimensional crystals. *Ultramicroscopy*, **14**, 319–336.
57. Frank, J., Shimkin, B. & Dowse, H. (1981). SPIDER—a modular software system for electron image processing. *Ultramicroscopy*, **6**, 343–358.
58. Philippsen, A., Schenk, A. D., Stahlberg, H. & Engel,

- 
- A. (2003). Iplt-image processing library and toolkit for the electron microscopy community. *J. Struct. Biol.* **144**, 4–12.
59. Saxton, W. O. (1996). Semper: distortion compensation, selective averaging, 3-D reconstruction, and transfer function correction in a highly programmable system. *J. Struct. Biol.* **116**, 230–236.
60. Collaborative Computational Project, N. (1994). The CCP4 Suite: Programs for Protein Crystallography. *Acta Crystallog. sect. D*, **50**, 760–763.

*Edited by Baumeister*

*(Received 24 August 2004; received in revised form 2 April 2005; accepted 15 April 2005)*